J|A|C|S
ARTICLES
Published on Web 10/01/2003

The Plumber's Nightmare:[1] A New Morphology in Block Copolymer−Ceramic Nanocomposites and Mesoporous Aluminosilicates

Adam C. Finnefrock,[‡,||] Ralph Ulrich,[§,⊥] Gilman E. S. Toombes,[‡] Sol M. Gruner,[‡] and Ulrich Wiesner*[,†]

Contribution from the Department of Materials Science and Engineering, 329 Bard Hall, Cornell University, Ithaca, New York 14853-1501, Physics Department, Cornell University, Clark Hall, Ithaca, New York 14853-2501, and Max-Planck-Institute for Polymer Research, Postfach 3148, D-55021 Mainz, Germany

Received April 7, 2003; E-mail: ubw1@cornell.edu

Abstract: A novel cubic bicontinuous morphology is found in polymer−ceramic nanocomposites and mesoporous aluminosilicates that are derived by an amphiphilic diblock copolymer, poly(isoprene-*b*-ethylene oxide) (PI-*b*-PEO), used as a structure-directing agent for an inorganic aluminosilicate. Small-angle X-ray scattering (SAXS) was employed to unambiguously identify the $Im\bar{3}m$ crystallographic symmetry of the materials by fitting individual Bragg peak positions in the two-dimensional X-ray images. Structure factor calculations, in conjunction with results from transmission electron microscopy, were used to narrow the range of possible structures consistent with the symmetry and showed the plumber's nightmare morphology to be consistent with the data. The samples are made by deposition onto a substrate that imposes a strain field, generating a lattice distortion. This distortion is quantitatively analyzed and shown to have resulted in shrinkage of the crystallites by approximately one-third in a direction perpendicular to the substrate, in both as-made composites and calcined ceramic materials. Finally, the observation of the bicontinuous block-copolymer-derived hybrid morphology is discussed in the context of a pseudo-ternary morphology diagram and compared to existing studies of ternary phase diagrams of amphiphiles in a mixture of two solvents. The calcined mesoporous materials have potential applications in the fields of catalysis, separation technology, and microelectronics.

Introduction

The field of organic−inorganic nanocomposite materials has been widely recognized as one of the most promising and rapidly emerging research areas in materials chemistry.[2] Novel structural features, physical properties, and complex functions are synergistically produced in these hybrids through the spatial organization of dissimilar and often incompatible components. This translates into enormous technological promise, and, indeed, new applications have already been realized or are expected in a wide range of areas.[3]

One key issue in the design of organic−inorganic hybrid materials is tailoring the interface between organic and inorganic components. Figure 1 summarizes a number of ways the interface can be varied in polymer−inorganic nanocomposites. Figure 1a reflects the interface between a homopolymer and an inorganic component (hatched area) that interact only weakly, for example, through van der Waals interactions. In Figure 1b, a polymer chain interacts through specific sites along the backbone, for example, the chain ends, with the inorganic material (tethered chains). Figure 1c shows a block copolymer for which only one block has specific interactions with the inorganic component. Finally, in Figure 1d, a scenario for a block copolymer chain is depicted for which one block is fully incorporated into the inorganic, thereby becoming an integral part of the inorganic phase of the material. Passing from Figure

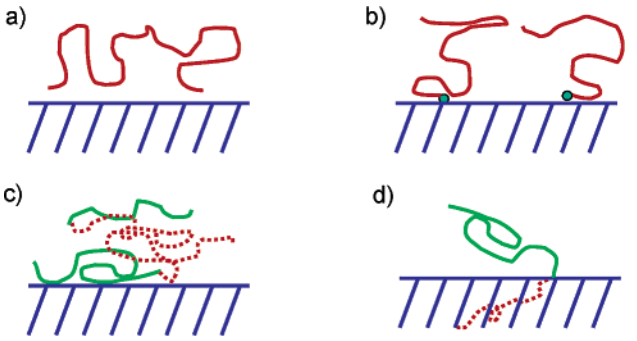

Figure 1. Different ways the interface can be varied in polymer−inorganic nanocomposites, as described in the text. Hatched areas represent inorganic materials.

† Department of Materials Science and Engineering, Cornell University.
‡ Physics Department, Cornell University.
§ Max-Planck-Institute for Polymer Research.
|| Current address: Merck Research Laboratories, WYN-2, 466 Devon Park Drive, Wayne, PA 19087-1816.
⊥ Current address: Bayer AG, Geschäftsbereich Kunststoffe, Abteilung KU - FE/TKT Gebäude R 33, D - 47812 Krefeld, Germany.

(1) Huse, D. A.; Leibler, S. *J. Phys.* **1988**, *49*, 605−620.
(2) Eckert, H.; Ward, M. *Chem. Mater.* **2001**, *13*, 3059−3060.
(3) For example, see contributions on *Hybrid Organic−Inorganic Materials* to: *MRS Bull.* **2001**, *26*, No. 5.

10.1021/ja0355170 CCC: $25.00

1a to 1d, the interactions between organic and inorganic components gradually increase. Integrating whole sections of a polymer chain into the inorganic phase (Figure 1d) evidently can be expected to have significant effects on structure, order, and dynamics of both components, ultimately leading to strong alterations of materials properties at the macroscopic length scale with respect to those of the pure components. Examples for the first two scenarios are found, for example, in the study of polymer−clay nanocomposites.[4,5] An example for Figure 1c is the block copolymer controlled growth of inorganic crystals.[6] The scenario of Figure 1d will be discussed in more detail below.

A second key issue determining the property profile of organic−inorganic hybrids is the control of shape and structure from the nanometer scale all the way to the macroscopic length scale. Self-assembly is often used for periodic nanostructures, frequently employing surfactant or copolymer structure-directing agents. Among the various possible polymer architectures, block copolymers are particularly promising because their phase behavior has been studied thoroughly for over 30 years and is relatively well understood.[7] To the best of our knowledge, the use of block copolymers as structure-directing agents started in the first half of the 1990s: block copolymers were first used to stabilize inorganic metal or semiconductor nanoparticles.[8−15] Bagshaw et al. subsequently used block-type low-molecular weight nonionic surfactants as templating agents to produce mesoporous molecular sieves.[16] The transition from the small to the large mesoscopic regime of silica type mesostructures/mesoporous materials was achieved during the second half of the 1990s.[17−19] More recently, Raez et al. demonstrated the formation of novel organometallic nanotubes by the self-assembly of a poly(ferrocenyldimethylsilane-*b*-dimethylsiloxane) block copolymer.[20] Stupp et al. successfully employed block-copolymer-type peptide amphiphiles for the mineralization of inorganic crystals.[21]

We have shown that working from organic solvents and by the appropriate choice of block copolymer, that is, poly(isoprene-*block*-ethyleneoxide) (PI-*b*-PEO), as well as ceramic precursor chemistry, that is, organically modified ceramic precursors (ormocers), dramatic morphology control is obtained on the nanoscale.[18,22] It is based on a polymer−ceramic interface that was characterized in detail by solid-state NMR measurements.[23] The hydrophilic parts of the block copolymers are completely integrated into the ceramic phase, as illustrated in Figure 1d. Because of the plasticizing effect of the polymer chains on the ceramic, we refer to these novel materials as "flexible ceramic nanocomposites". The resulting composites can be described as quasi two-phase systems allowing for a rational hybrid morphology design based upon the current understanding of the phase behavior of block copolymers and copolymer−homopolymer mixtures.[7] Indeed, most of the mesophase morphologies known for block copolymers or copolymer−homopolymer mixtures have now been explored in the bulk synthesis of these block-copolymer−ceramic hybrid materials.[22]

The composite materials exhibit a broad spectrum of potential applications. After calcinations at elevated temperature, they form mesoporous materials with pore sizes expanding into the tens of nanometer regime (see below), proving relevant to the field of separations technology and catalysis.[22,24] Earlier, we demonstrated that the hybrids can be used to generate "hairy" nanoobjects with controlled shape, size, and composition.[25] These nanoparticles can subsequently be mixed into block copolymers, thereby preparing model nanocomposites with fillers of well-controlled dimensionality and surface characteristics.[26] These systems, for example, may help to better understand the polymer physics of nanocomposites, an area of enormous technological importance. Furthermore, we have shown that doping the composites with a lithium salt leads to a novel type of lithium ion conductors, referred to as solid hybrid polymer (SHyP) electrolytes.[24,27] The materials exhibit a novel combination of properties and illustrate possible avenues toward hybrid materials for battery and fuel cell applications.

One of the most intriguing aspects of block copolymer and surfactant polymorphism is the existence of ordered bicontinuous phases. It seems established at the present[7] that for single-component diblock copolymers the stable phase that has been observed is invariably the bicontinuous double gyroid, with $Ia\bar{3}d$ symmetry.[28] For the "ormocer" derived hybrid materials described above, we have recently discovered the existence of a novel block-copolymer-based bicontinuous structure with $Im\bar{3}m$ symmetry, a symmetry class that includes the "plumber's nightmare" morphology.[29] It is important to recall that many structures are consistent with any given symmetry. As in the case of amphiphilic systems, once the space group is rigorously established, there is still the question as to the specific structure of the material, even if it is assumed that the structure is of the type that may be derived from a minimal surface.[28,30] In this

(4) Vaia, R. A.; Giannelis, E. P. *MRS Bull.* **2001**, *26*, 394−401.
(5) Weimer, M. W.; Chen, H.; Giannelis, E. P.; Sogah, D. Y. *J. Am. Chem. Soc.* **1999**, *121*, 1615−1616.
(6) Marentette, J. M.; Norwig, J.; Stockelmann, E.; Meyer, W. H.; Wegner, G. *Adv. Mater.* **1997**, *9*, 647−651.
(7) Hamley, I. W. *The Physics of Block Copolymers*; Oxford University Press: Oxford, 1998.
(8) Sankaran, V.; Cummins, C. C.; Schrock, R. R.; Cohen, R. E.; Silbey, R. J. *J. Am. Chem. Soc.* **1990**, *112*, 6858−6859.
(9) Chan, Y. N. C.; Schrock, R. R.; Cohen, R. E. *Chem. Mater.* **1992**, *4*, 24−27.
(10) Moffitt, M.; Eisenberg, A. *Chem. Mater.* **1995**, *7*, 1178−1184.
(11) Spatz, J. P.; Roescher, A.; Sheiko, S.; Krausch, G.; Moller, M. *Adv. Mater.* **1995**, *7*, 731−735.
(12) Antonietti, M. W., E.; Bronstein, L.; Seregina, M. *Adv. Mater.* **1995**, *7*, 1000.
(13) Clay, R. T.; Cohen, R. E. *Supramol. Sci.* **1996**, *2*, 183.
(14) Kane, R. S.; Cohen, R. E.; Silbey, R. *Chem. Mater.* **1996**, *8*, 1919−1924.
(15) Braun, P. V.; Osenar, P.; Stupp, S. I. *Nature* **1996**, *380*, 325−328.
(16) Bagshaw, S. A.; Prouzet, E.; Pinnavaia, T. J. *Science* **1995**, *269*, 1242−1244.
(17) Antoniette, M.; Göltner, C. *Angew. Chem., Int. Ed.* **1997**, *36*, 910.
(18) Templin, M.; Franck, A.; DuChesne, A.; Leist, H.; Zhang, Y. M.; Ulrich, R.; Schadler, V.; Wiesner, U. *Science* **1997**, *278*, 1795−1798.
(19) Zhao, D. Y.; Feng, J. L.; Huo, Q. S.; Melosh, N.; Fredrickson, G. H.; Chmelka, B. F.; Stucky, G. D. *Science* **1998**, *279*, 548−552.
(20) Raez, J.; Barjovanu, R.; Massey, J. A.; Winnik, M. A.; Manners, I. *Angew. Chem., Int. Ed.* **2000**, *39*, 3862.
(21) Hartgerink, J. D.; Beniash, E.; Stupp, S. I. *Science* **2001**, *294*, 1684−1688.
(22) Simon, P. F. W.; Ulrich, R.; Spiess, H. W.; Wiesner, U. *Chem. Mater.* **2001**, *13*, 3464−3486.
(23) De Paul, S. M.; Zwanziger, J. W.; Ulrich, R.; Wiesner, U.; Spiess, H. W. *J. Am. Chem. Soc.* **1999**, *121*, 5727−5736.
(24) Ulrich, R. *Morphologien und Eigenschaften strukturierter organisch-anorganischer Hybridmaterialien*; Logos-Verlag: Berlin, 2000.
(25) Ulrich, R.; Du Chesne, A.; Templin, M.; Wiesner, U. *Adv. Mater.* **1999**, *11*, 141−146.
(26) Jain, A.; Gutmann, J. S.; Garcia, C. B. W.; Zhang, Y. M.; Tate, M. W.; Gruner, S. M.; Wiesner, U. *Macromolecules* **2002**, *35*, 4862−4865.
(27) Ulrich, R.; Zwanziger, J. W.; De Paul, S. M.; Reiche, A.; Leuninger, H.; Spiess, H. W.; Wiesner, U. *Adv. Mater.* **2002**, *14*, 1134−1137.
(28) Hajduk, D. A.; Harper, P. E.; Gruner, S. M.; Honeker, C. C.; Kim, G.; Thomas, E. L.; Fetters, L. J. *Macromolecules* **1994**, *27*, 4063−4075.
(29) Finnefrock, A. C.; Ulrich, R.; Du Chesne, A.; Honeker, C. C.; Schumacher, K.; Unger, K. K.; Gruner, S. M.; Wiesner, U. *Angew. Chem., Int. Ed.* **2001**, *40*, 1208.
(30) Strom, P.; Anderson, D. M. *Langmuir* **1992**, *8*, 691−709.

Scheme 1. Diblock Copolymer Poly(isoprene-*b*-ethyleneoxide) (PI-*b*-PEO) Is Added to an 80:20 Mixture (Molar Ratio) of Ormocer Precursors (3-Glycidyloxypropyl)-trimethoxysilane (GLYMO) and Aluminum *sec*-Butoxide

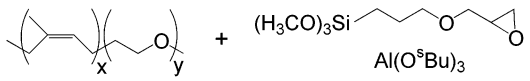

paper, we use small-angle X-ray scattering (SAXS) to unambiguously identify the crystallographic symmetry and then use information from the intensities of the Bragg reflections to narrow the range of possible structures. We also analyze a distortion of the lattice in terms of a strain field arising from the synthesis of the material. Finally, the observation of the bicontinuous block-copolymer-derived hybrid morphology is discussed in the context of a pseudo-ternary morphology diagram and compared to existing studies of ternary phase diagrams of amphiphiles in a mixture of two solvents.

Experimental Section

An amphiphilic diblock copolymer poly(isoprene-*b*-ethyleneoxide) (PI-*b*-PEO) with a total number average molecular weight, M_n, of 16 400 g/mol and a weight fraction of PEO of 38% (PEO $M_n = 6200$ g/mol) was used as the structure-directing agent. Anionic polymerization was employed to generate this polymer with a narrow molecular weight distribution of 1.07.[31] In the bulk, above the melting of the crystalline lamellar phase, the pure diblock copolymer exhibits a morphology of hexagonally packed PEO cylinders in a PI matrix.[7,32] A film of the organic−inorganic hybrid material with a thickness of about 1 mm was prepared by mixing of the ormocer precursors (3-glycidyloxypropyl)-trimethoxysilane (GLYMO) and aluminum *sec*-butoxide in a molar ratio of 80:20 and subsequent combination with the diblock copolymer in organic solvents (Scheme 1), as described in earlier publications.[18,22,25]

The volume fraction of the PI phase of the as-made material was calculated to be 0.36 (weight % of PI in the as-made hybrid sample after synthesis was 26.8%). It is assumed that there is negligible phase mixing between the PI (density 0.91 g/cm^3) and the inorganic/PEO microphases (density 1.4 g/cm^3).[23] The organic−inorganic nanocomposite was then calcined to obtain a mesoporous material. Calcination was achieved by heating in several stages up to 600 °C in air with an overall heating rate of approximately 1 °C/min. Elemental analysis after calcination indicated C, 0.1 wt %, and H, 1.5 wt %. The weight loss, measured by thermogravimetric analysis (TGA) as 75%, compared well with the theoretical prediction of 78%. As described in the first communication, analysis of nitrogen adsorption/desorption isotherms by the BET-method revealed a pore surface area of 300 m^2/g.[29]

The synthesis of a hybrid sample with morphology consistent with the plumber's nightmare (see below) was repeated starting from the same block copolymer but for an as-made composite with calculated PI volume fraction of 0.35 (weight % of PI in the as-made hybrid sample after synthesis was 25.5%). For comparison with hybrid samples with $Im\bar{3}m$ symmetry, a PI-*b*-PEO block copolymer exhibiting a double gyroid morphology with $Ia\bar{3}d$ symmetry was also studied using SAXS, see below. This block copolymer had a total number average molecular weight, M_n, of 10 400 g/mol and a weight fraction of PEO of 51% (PEO $M_n = 5000$ g/mol). It showed the double gyroid structure at temperatures between 120 and 230 °C.[32] The SAXS results shown in this paper (see Figure 3) were obtained at 180 °C.

For TEM, the uncalcined organic−inorganic hybrid sample was used as synthesized. The calcined sample was manually powdered and embedded in UHU-Glue (Henkel). Ultrathin sections (50−100 nm thick) were produced using a Leica-Ultramicrotome (UCT) at 218 K. Sections were floated off the diamond knife onto aqueous DMSO solution, transferred to grids, and investigated unstained. TEM was performed on a Leo 912 Ω (tungsten filament) microscope operated at 120 kV using an objective aperture angle of 16.5 mrad. All images were taken in the elastically filtered imaging mode. Contrast of the unstained, as-made samples was very weak, but the morphology of the samples could be clearly observed at a defocus of approximately 2.5 μm. The organic−inorganic (aluminosilicate) hybrid appears as the dark phase. Images were recorded using a slow scan CCD camera (lateral resolution 1 K × 1 K pixels, 14-bit gray values).

X-ray data were acquired both at a rotating-anode source and at the D-1 station of the Cornell High Energy Synchrotron Source (CHESS). The rotating-anode source consisted of a Rigaku RU300 copper rotating anode generator ($\lambda = 1.54$ Å) with Ni filter and orthogonal Franks focusing mirrors. Samples were examined by SAXS before and after calcination. Small single pieces of film from each batch were placed in glass X-ray capillaries; large samples (approximately 1 cm^2) were mounted in air with sticky tape. Rotation series were collected in steps as small as 1°. In all cases, SAXS patterns were recorded with home-built 1 K × 1 K pixel CCD detectors[33,34] and calibrated accordingly.[35] The q-dimensions of each image were calibrated with silver behenate[36,37] (lamellar repeat, $d = 58.376$ Å) and spherical calibrants[38,39] (radius, $R = 278$ Å). Further SAXS image analysis was performed with a suite of programs written in C and Matlab (Mathworks, Natick, MA).

Results and Discussion

Identification of the Space Group. Small-angle X-ray scattering (SAXS) is ideal for determining the symmetry group of complex structures. We have performed SAXS experiments on both as-made and calcined samples, shown in Figure 2. These samples were oriented such that the surface normal was within a few degrees of the X-ray beam propagation direction. The images indicate a high degree of order, out to $q^2 = h^2 + k^2 + l^2 = 50$ and $q^2 = 32$ reciprocal lattice units for the as-made and calcined samples, respectively. Because of the large dynamic range of the data set, the false color scale corresponds to the logarithm of the X-ray intensity.

For block copolymers and block-copolymer-derived materials, the results are typically scattering profiles of X-ray scattering intensity, I, versus the magnitude of the scattering vector $q = (4\pi/\lambda) \sin \theta$, where λ is the X-ray wavelength and 2θ is the scattering angle. Integrating the images in Figure 2a along the azimuthal direction (q_φ) and then normalizing each integral to a unit area of the detector results in the intensity profile shown in Figure 3b. For comparison, a diffraction pattern for a pure PI-*b*-PEO material consistent with $Ia\bar{3}d$ symmetry, thus suggesting a double gyroid morphology, is shown in Figure 3a. However, for the as-made hybrid material, the positions of the most intense and unambiguous peaks have been fit and have the distance ratios from the origin of reciprocal space of $\sqrt{2}:\sqrt{4}:\sqrt{6}:\sqrt{8}:\sqrt{14}$ (Figure 3b). This is also true for the

(31) Allgaier, J.; Poppe, A.; Willner, L.; Richter, D. *Macromolecules* **1997**, *30*, 1582−1586.
(32) Floudas, G.; Vazaiou, B.; Schipper, F.; Ulrich, R.; Wiesner, U.; Iatrou, H.; Hadjichristidis, N. *Macromolecules* **2001**, *34*, 2947−2957.
(33) Tate, M. W.; Eikenberry, E. F.; Barna, S. L.; Wall, M. E.; Lowrance, J. L.; Gruner, S. M. *J. Appl. Crystallogr.* **1995**, *28*, 196−205.
(34) Tate, M. W.; Gruner, S. M.; Eikenberry, E. F. *Rev. Sci. Instrum.* **1997**, *68*, 47−54.
(35) Barna, S. L.; Tate, M. W.; Gruner, S. M.; Eikenberry, E. F. *Rev. Sci. Instrum.* **1999**, *70*, 2927−2934.
(36) Huang, T. C.; Toraya, H.; Blanton, T. N.; Wu, Y. *J. Appl. Crystallogr.* **1993**, *26*, 180−184.
(37) Blanton, T. N.; Huang, T. C.; Toraya, H.; Hubbard, C. R.; Robie, S. B.; Louër, D.; Göbel, H. E.; Will, G.; Gilles, R.; Raftery, T. *Powder Diffr.* **1995**, *10*, 91−95.
(38) Megens, M.; van Kats, C. M.; Bosecke, P.; Vos, W. L. *J. Appl. Crystallogr.* **1997**, *30*, 637−641.
(39) Megens, M.; vanKats, C. M.; Bosecke, P.; Vos, W. L. *Langmuir* **1997**, *13*, 6120−6129.

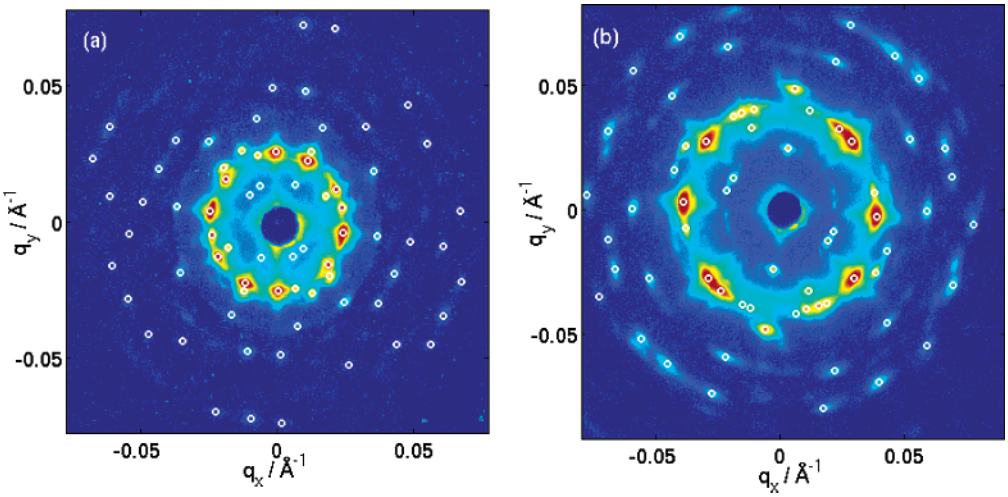

Figure 2. Rotating anode SAXS images obtained from (a) as-made and (b) calcined samples. The false color scale corresponds to logarithmic X-ray intensity. The as-made sample data were taken with 42 exposures over 9.3 h to maximize the signal-to-noise ratio and dynamic range. The calcined sample with considerably greater electron contrast only required 12 exposures totaling 18 min. The positions of bright Bragg peaks used in the fitting procedure (see Figure 4) are identified with superimposed circles.

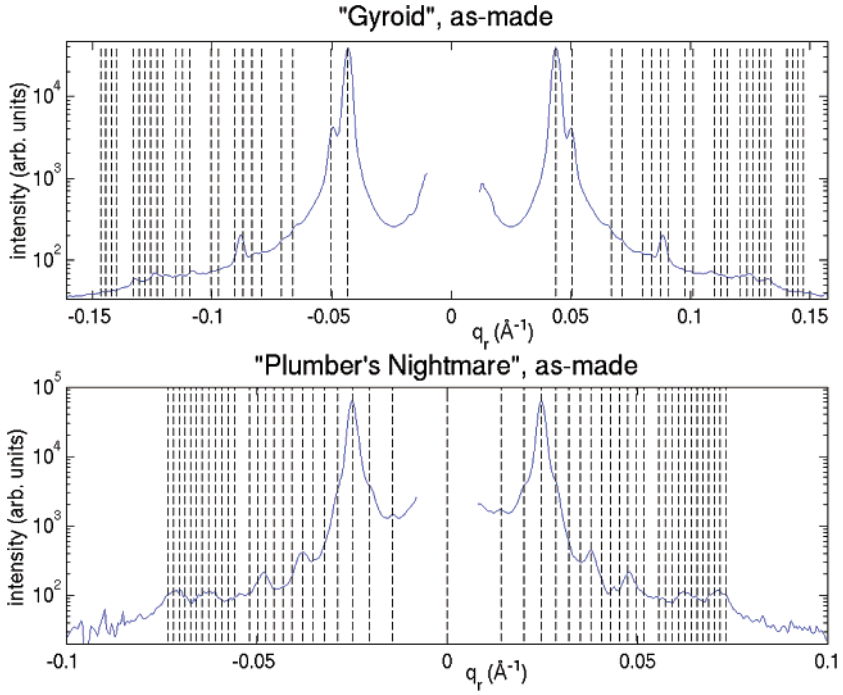

Figure 3. Measured scattering profile (X-ray intensity, I, vs scattering vector length, q) measured for (a) a pure PI-*b*-PEO block copolymer and (b) the as-made block-copolymer−ceramic hybrid discussed in this Article. The vertical lines correspond to the expected peaks for (a) $Ia\bar{3}d$ (consistent with a double gyroid morphology) and (b) $Im\bar{3}m$ (consistent with a plumber's nightmare morphology) crystallographic symmetries.

calcined hybrid material (not shown). These ratios are consistent with the $Im\bar{3}m$ space group.[28]

Azimuthally integrated one-dimensional scattering profiles of block copolymer materials are usually somewhat unsatisfactory for three reasons: First, different peaks overlap in a radial direction leading to a loss in resolution. For instance, the strong ⟨200⟩ peaks blend into the very strong ⟨211⟩. This problem is exacerbated at large q, where the intensities are lower and peaks tend to pile up. Second, weak peaks are hard to detect, because they are superimposed upon a background that is integrated over a full 2π in azimuth, leading to a poor signal-to-noise ratio. Third, peaks which are widely separated in q_φ but close in q_r will appear to overlap and be difficult to distinguish.

Often one-dimensional SAXS profiles are the only practical way to express the data, because either only linear detectors rather than area detectors are available or the SAXS diffraction patterns show no variation in the azimuthal direction ("pure powder rings"). However, our block-copolymer-derived materials are highly well-ordered, with single-crystal domains up to 100 μm.[29] As a result, we see superimposed diffraction patterns from a small number of single crystals, an intermediate case between a single crystal pattern and polycrystalline/powder patterns. The individual Bragg patterns provide additional information, provided that the peaks associated with each crystallite can be uniquely identified. By fitting the individual Bragg peak positions, we can place stronger constraints on the possible symmetry groups and obtain a lower limit on the number of domains contributing to the scattering pattern.

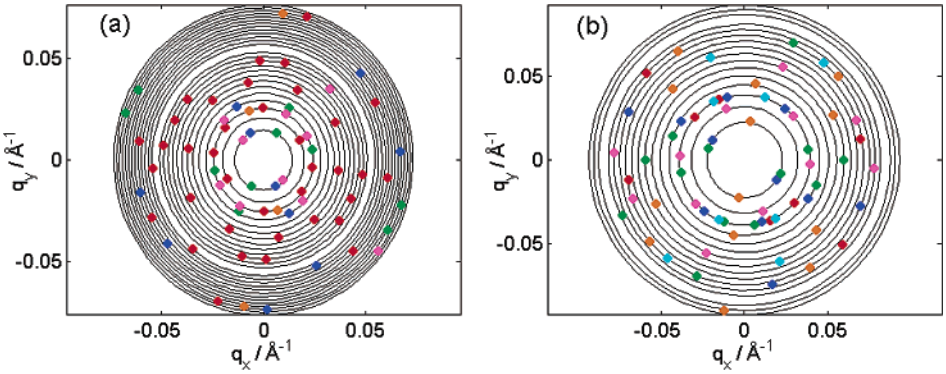

Figure 4. Indexed positions of peaks seen in the SAXS data of Figure 2 for (a) as-made and (b) calcined samples. All of these peaks can be assigned to five microdomains within the scattering volume for (a), and six microdomains for (b). Each peak is colored according to the microdomain with which it can be identified. The zone directions of the microdomains in (a) are yellow-751, magenta-311, green-110, blue-331, red-320; for (b) the zone directions are cyan-210, yellow-331, magenta-210, green-111, blue-433, red-421. The gap in the rings is obtained because $q^2 = 28$ reciprocal lattice units is not the sum of three squares ($h^2 + k^2 + l^2$).

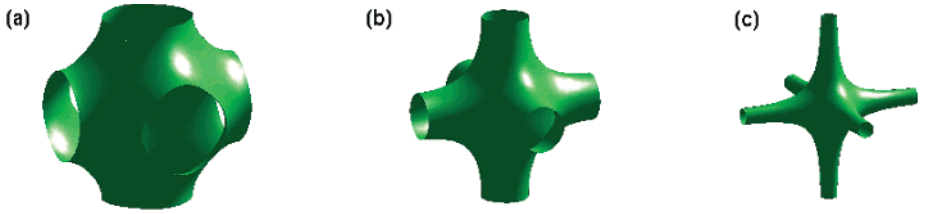

Figure 5. An example contrasting a minimal surface and its analogues: (a) P, plumber's nightmare minimal surface, (b) P constant mean curvature surface, and (c) P skeletal surface.

However, this approach is more challenging (see below) than the fitting of data from the limiting cases of powder rings or single-crystal specimens.

For each SAXS image in Figure 2, peaks were identified by eye and their positions were determined by computing their centroids; these are plotted in Figure 4. Peaks were identified according to the following procedure: each pair of peaks was assigned all possible pairs of Miller indices ($h_1k_1l_1$), ($h_2k_2l_2$), which were consistent with their radial position $q_r = \sqrt{h^2+k^2+l^2}$. From each resulting orientation matrix, the positions of other peaks that fell on the Ewald sphere and were allowed by the symmetry group were calculated. The number of additional matching peaks was tabulated, and the orientation matrix that fit the most peaks was then chosen. The entire procedure was then repeated recursively for the remaining pairs of peaks until all peaks could be assigned to the minimal number of domains. At the end, an orientation matrix had been assigned to each crystallite within the scattering volume. The result is shown in Figure 4, wherein the peaks have been colored according to the single-crystal microdomain; the peaks circled in Figure 2 can be explained by five microdomains within the as-made image, and six microdomains within the calcined image. This is a reasonable result given the X-ray beam area (1 mm^2) and a domain size on the order of 0.1 mm^2.

From this analysis, we estimate a lattice spacing in the plane of the sample film of 630 Å for the as-made sample and 395 Å for the calcined sample. It is striking that the order and symmetry are so well-preserved under calcination even though the lattice constant falls to approximately 60% of its as-made value and the cell volume falls to approximately 25%. This indicates that the bonding network formed by the inorganic component is extremely robust, which may be a general advantage of the present diblock-copolymer directed organically modified ceramic (ormocer) materials.

Minimal Surface Morphologies. Minimal surfaces (Figure 5a) minimize the interfacial area between two volumes. In the present context, the minimal surfaces of interest divide two interpenetrating volumes and everywhere on the surface there is zero mean curvature (i.e., the average of the two principal curvatures). Minimal surfaces typically occur in nature in cases where a dominant term in the interfacial free energy increases with the contact area of two dissimilar materials. They have been found in a wide variety of surfactant−water and lipid−water mixtures. In these systems, the surfactant forms a complex, multiconnected bilayer in which a zero-mean curvature surface represents the dividing surface in the middle of the bilayer.[40,41] The two surfaces displaced on either side from the minimal surface by the thickness of the surfactant monolayers are surfaces representing the positions of the surfactant headgroups. These surfaces are near-constant-curvature surfaces.[42] The near-constant-curvature surfaces divide space into three volumes: between the headgroup surfaces is the surfactant bilayer, and on either side of the bilayer are two distinct but congruent multiply connected water volumes. These water volumes are, therefore, bicontinuous throughout the structure (see Figure 7).

Bicontinuous block copolymer phases can be related to surfactant−water bicontinuous phases with the minority block playing the role of the surfactant bilayer and the majority block playing the role of the water. However, block copolymer systems impose the additional constraint that the local volume of the two blocks must be nearly conserved because the two blocks are joined. In these cases, the surfaces separating the block microdomains may be considerably distorted from the shape of near-constant-curvature surfaces. This may be done without

(40) Gruner, S. M. *J. Phys. Chem.* **1989**, *93*, 7562−7570.
(41) Seddon, J. M.; Templer, R. H. *Philos. Trans. R. Soc. London* **1993**, *344*, 377−401.
(42) Anderson, D.; Gruner, S. M.; Leibler, S. *Proc. Natl. Acad. Sci. U.S.A.* **1988**, *85*, 5364−5368.

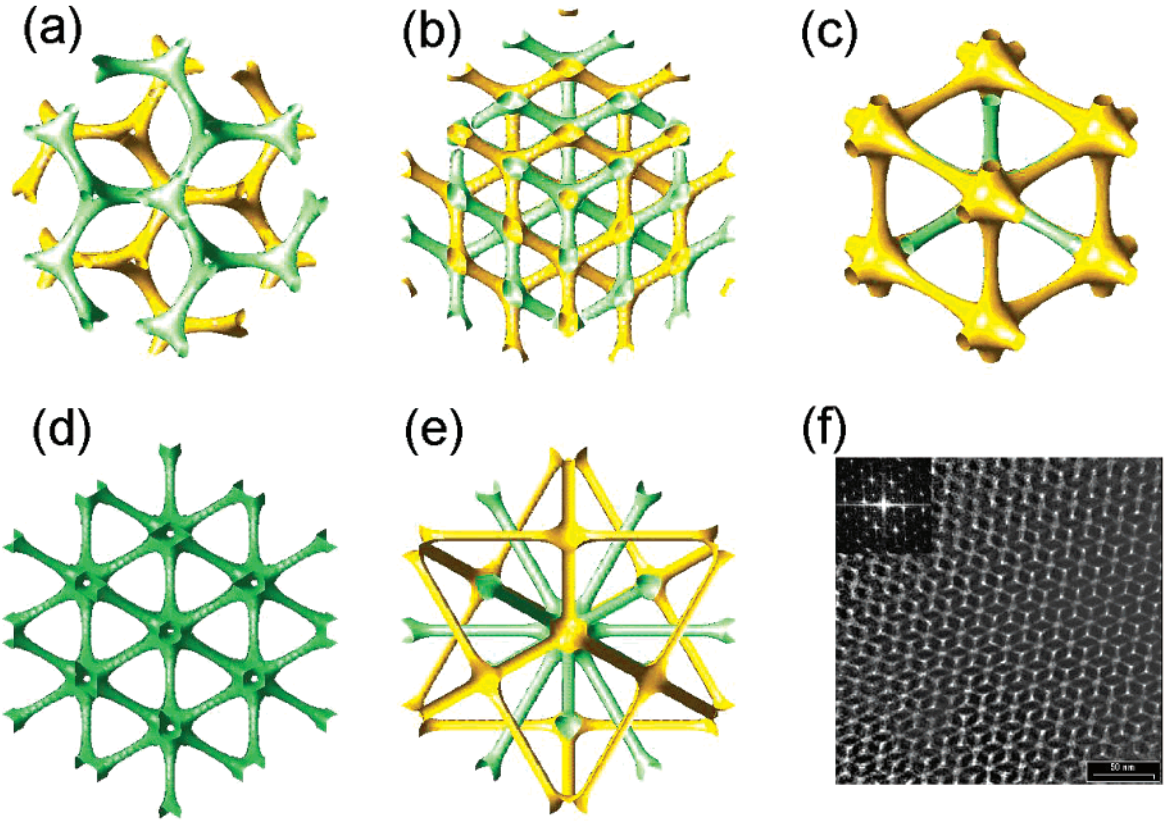

Figure 6. (111) orientations of the (a) double gyroid, (b) double diamond, (c) plumber's nightmare, (d) I-WP, (e) Neovius' surfaces, and (f) TEM "wagon-wheel" pattern from the calcined material. The Neovius surface is incompatible with the TEM data.

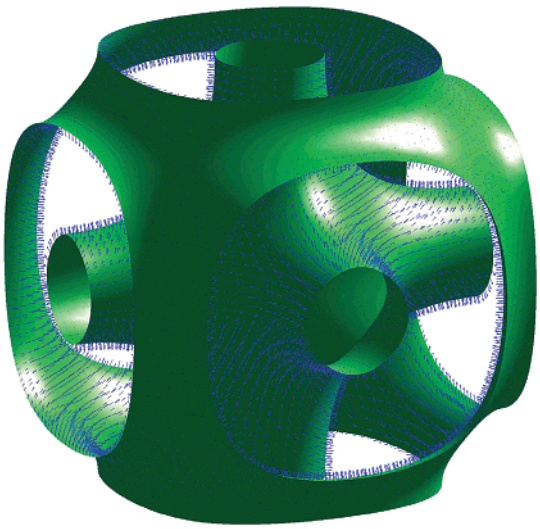

Figure 7. Illustration of the structure factor calculation for one unit cell of the plumber's nightmare morphology. The volume integral is converted to a surface integral using Gauss' divergence theorem. The small blue arrows correspond to surface normals used in the integration. (The actual number of integration points is far more numerous than illustrated here.) The complementary surface is displayed as the connected "cage" around its dual surface located in the center.

changing the crystallographic symmetry or connectivity of the microphase separated domains, as for example, shown in Figure 5. Figure 5a shows the P minimal surface, also known as the plumber's nightmare minimal surface. In Figure 5b, a constant mean curvature surface is shown. For the purposes of visualizing complex structures, it is convenient to continuously and smoothly distort by shrinking the minority volume fraction to near zero. The result is two networks of thin rods joined together with the same topology and coordination of the parent minimal structure; these are called skeletal graphs (Figure 5c).

We will consider the PI-*b*-PEO directed hybrid materials in terms of continuous and bicontinuous surfaces based upon five elementary minimal surfaces. These minimal surfaces generate the double gyroid, double diamond, (double) plumber's nightmare, I-WP, and Neovius surfaces,[43,44] the skeletal surfaces of which are shown in Figure 6. Although more minimal surfaces can be generated, they have higher interfacial surface areas and correspondingly higher energies. For these reasons, we confine our analysis to the consideration of these five structures above.

The identification of a structure as derived from a minimal surface requires satisfying a stringent set of criteria. First, there must be some indication that the morphology resembles a connected continuous or bicontinuous structure, as opposed to spheres or cylinders, for example. Second, the symmetry group determination must be consistent with the morphology in question. Third, in the case of multiple structural morphologies with identical symmetry groups, additional evidence must be obtained either by electron microscopy or by detailed scattering structure factor calculations to identify the correct structure.

Because the double gyroid ($Ia\bar{3}d$) and double diamond ($Pn\bar{3}m$) morphologies do not have $Im\bar{3}m$ symmetry, these are inconsistent with the SAXS data. However, the determination of the symmetry group alone is insufficient to distinguish between the

(43) A wealth of information may be found in the reports from the International Workshop on Geometry and Interface, Aussois, France, Sept 17−22, 1990, collected in *Colloque de Physique*, 1990; Coll. C7, supp. No. 23, Vol. 51. See especially: Hyde, S. T. pp C7-209−C7-228 in this volume.

(44) See the abundance of material as part of The Scientific Graphics Project, http://www.msri.org/publications/sgp/SGP/indexc.html.

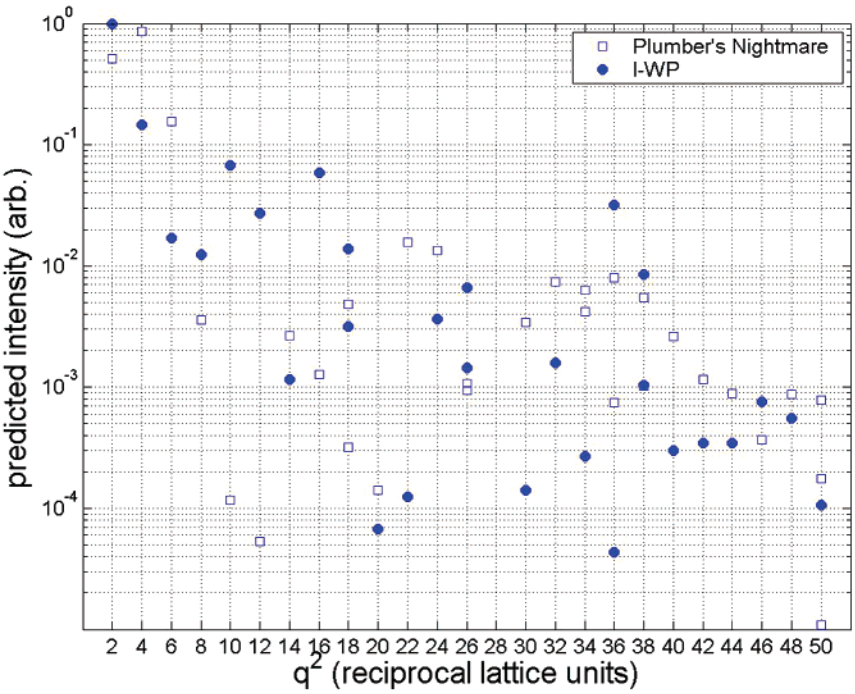

Figure 8. Predicted intensities based upon structure factors for the plumber's nightmare (□) and I-WP (●) morphologies. Note the very depressed intensities for $q^2 = 10,12$ for the plumber's nightmare consistent with its persistent absence or suppression in the experimental SAXS data.

remaining morphologies (plumber's nightmare, I-WP, Neovius) that all have $Im\bar{3}m$ symmetry.

TEM Data. Figure 6f shows a bright-field TEM of the calcined material. Bright areas correspond to voids in the structure, while dark areas correspond to solid material. From this image, we can see thin, connected volumes ("wagon-wheel" structure) with a high degree of symmetry and order over large domains (up to 100 μm). Earlier micrographs[29] illustrate the classic four-fold and three-fold orientations, which also have been traditionally associated with the double gyroid morphology. The skeletal representations in Figure 6 show that the plumber's nightmare and I-WP morphologies can both produce similar TEM patterns if viewed along certain crystallographic directions. TEM data alone without a full three-dimensional reconstruction cannot distinguish between these different morphologies. The Neovius structure can, however, be excluded by its projection that contains too many spokes at the wrong angles. The combination of SAXS and TEM data together thus suggests only two candidate structures: the plumber's nightmare and I-WP.

Structure Factor. Although the TEM image shown here suggests bicontinuity, due to the difficulty of interpreting TEM images, no definitive comparison was made between plumber's nightmare and I-WP morphologies on the basis of the TEM images alone. Further information could be obtained, however, from analysis of the two-dimensional X-ray images. Ideally, the Bragg peaks could be integrated and used to solve the structure. However, this was difficult because the large mosaic spread of the sample indicated that the Bragg peaks were only partially recorded and many peaks overlapped at their edges. Powder pattern analysis is excluded because a powder would contain numerous crystallites with different basis vectors (see following sections) which would make the task of deciphering the data extremely difficult. However, the consistent lack of observation of certain peaks (such as $q^2 = 10,12$; see Figures 3 and 4) points to a suppression of the corresponding Bragg peaks by the structure factor. To see whether the plumber's nightmare or I-WP structure was more consistent with the data, the structure factor $S(\mathbf{q}) = \int d\mathbf{r} \exp(-i\mathbf{q}\cdot\mathbf{r})\rho(\mathbf{r})$ was calculated from each morphology. An example of this analysis is shown for the plumber's nightmare structure in Figure 7. The electronic density $\rho(\mathbf{r})$ was determined as follows: constant mean curvature surfaces were generated using the Evolver program,[45] numerically minimizing the interfacial area between PI and PEO/inorganic phases while holding the phase volume ratio constant. The ratio of volumes was equal to those described in the Experimental Section. Level sets[46] of special periodic functions were also used for computational convenience, after comparison to ensure identity with the numerical minimization results. We also compared the I−WP minimal surfaces (generated analytically via Flächenstücke[47,48]) to the P by relaxing the local volume constraint.

As shown in Figure 8, the plumber's nightmare structure has a very low magnitude structure factor at $q^2 = 10,12$, while the I-WP morphology has values approximately 600−700 times greater. As these peaks are not observed across thousands of images, in both as-made and calcined samples, the strong intensities from I-WP are inconsistent with the data, suggesting that the candidate morphology is the plumber's nightmare. It should be noted that an alternate way to identify the relevant structure is to combine SAXS with three-dimensional TEM tomography.[49−51]

(45) Brakke, K. A. *Exp. Math.* **1992**, *1*, 141−165.
(46) Thomas, E. L.; Anderson, D. M.; Henkee, C. S.; Hoffman, D. *Nature* **1988**, *334*, 598−601.
(47) Andersson, S.; Hyde, S. T.; Larsson, K.; Lidin, S. *Chem. Rev.* **1988**, *88*, 221.
(48) Harper, P. E. *Physics Department*; Princeton University: Princeton, NJ, 1996.
(49) Spontak, R. J.; Fung, J. C.; Braunfeld, M. B.; Sedat, J. W.; Agard, D. A.; Kane, L.; Smith, S. D.; Satkowski, M. M.; Ashraf, A.; Hajduk, D. A.; Gruner, S. M. *Macromolecules* **1996**, *29*, 4494−4507.

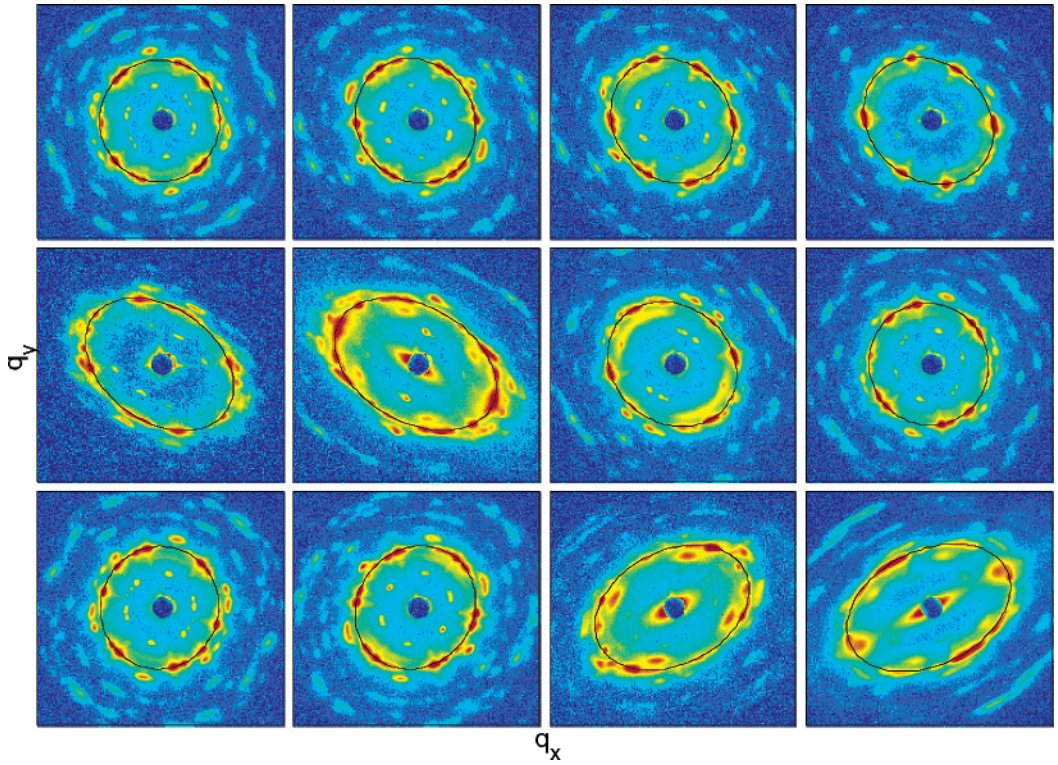

Figure 9. A sequence of SAXS images taken from the calcined sample at different values of the rotation angle ϕ (rotation axis along the q_y direction). The thin black ellipses are determined by least-squares fits to the ⟨211⟩ peak positions. A movie containing a complete rotation sequence is provided in the Supporting Information (rotation-data.avi).

Elliptical Pattern Analysis. The SAXS data shown above were for sample orientations such that the X-ray beam was nearly collinear with the normal to the sample face. Careful analysis of the positions in Figure 4 indicates that they do not lie on perfectly circular rings. Rather, the rings are slightly eccentric, with major/minor axis ratios of 1.04 (as-made) and 1.07 (calcined). The major axis lies in the q_y direction, parallel to the axis about which the sample was rotated. As the sample is rotated, the ratio of semimajor and semiminor axes (a/b or eccentricity) increases. Simultaneously, the angle between the semimajor axis and q_y (θ_0) increases markedly. The stretching and rotation of the ellipse becomes quite dramatic for large rotation angles as shown in Figure 9. (These are a subset of the rotation data, a movie of which is available in the Supporting Information.)

The experimental findings can be explained using the following model. The samples were cast from thin films where solvent was slowly allowed to evaporate. This introduces an anisotropic strain field in the sample such that the dimension perpendicular to the substrate is reduced relative to the two other dimensions parallel to the substrate, as depicted in Figure 10.[52] In other words, the film shrinks in thickness but shrinks relatively very little in lateral extent. The strain applies to each crystal domain, regardless of its crystallographic orientation relative to the substrate: the significant factor is the macroscopic shape, which is dominated by the boundary conditions imposed by the substrate during solvent evaporation. As a consequence, each domain is deformed along a single macroscopic axis (uniaxial deformation, as depicted in Figure 10b), which has no particular registry with the crystallographic axes of any particular domain. This real-space contraction leads to an overall elongation in reciprocal space (Figure 10b).

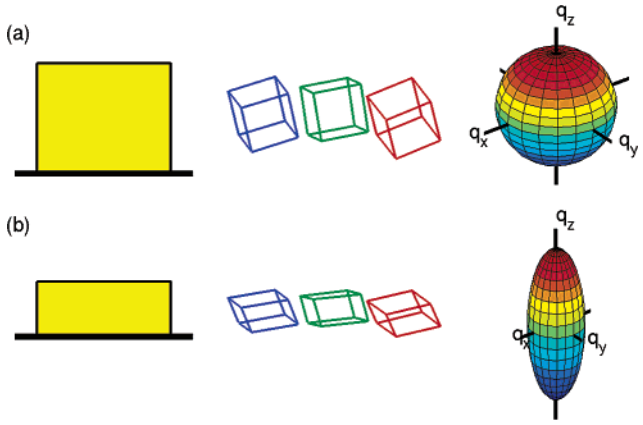

Figure 10. Cartoon of sample contraction and its effect upon reciprocal space structure. (a) Ideal isotropic case. The sphere represents the surface in reciprocal space containing all of the Bragg reflections at a constant value of $h^2 + k^2 + l^2$. For a lattice with cubic symmetry, many Bragg reflections share common spheres. (b) Contraction along one real-space axis perpendicular to the substrate produces an elongation of the reciprocal space sphere, irrespective of the crystal orientation of each domain.

An ideal powder of a sample with cubic symmetry would be expected to have a Fourier transform in three-dimensional reciprocal space that took the form of concentric spherical shells. For instance, a powder where each domain had $Im\bar{3}m$ symmetry would produce spheres in reciprocal space of radii $q = \sqrt{2},\sqrt{4},\sqrt{6},\sqrt{8},...$ A perfect single crystalline sample of the

(50) Laurer, J. H.; Hajduk, D. A.; Fung, J. C.; Sedat, J. W.; Smith, S. D.; Gruner, S. M.; Agard, D. A.; Spontak, R. J. *Macromolecules* **1997**, *30*, 3938−3941.
(51) Sakamoto, Y. H.; Kaneda, M.; Terasaki, O.; Zhao, D. Y.; Kim, J. M.; Stucky, G.; Shim, H. J.; Ryoo, R. *Nature* **2000**, 449−453.
(52) Klotz, M.; Albouy, P.-A.; Ayral, A.; Menager, C.; Grosso, D.; Van der Lee, A.; Cabuil, V.; Babonneau, F.; Guizard, C. *Chem. Mater.* **2000**, *12*, 1721.

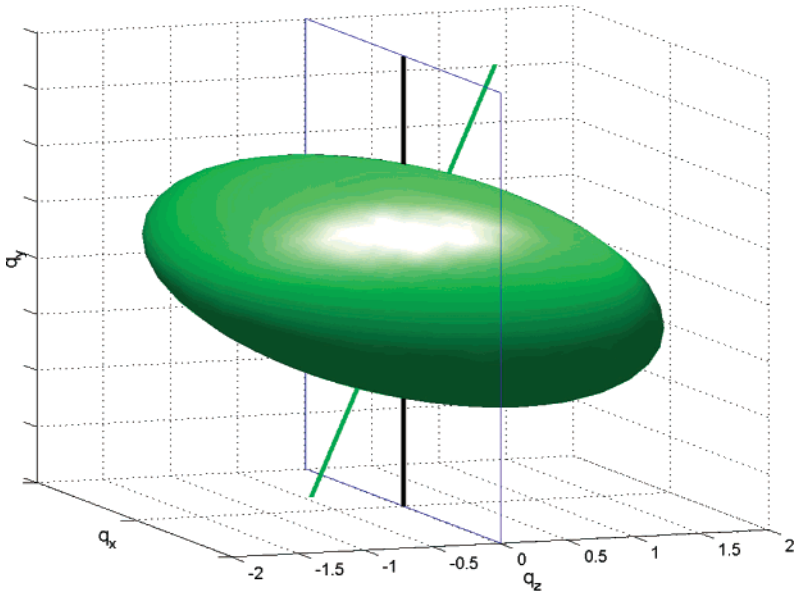

Figure 11. Prolate spheroid from Figure 10b with the rotation axis and Ewald plane. The observed SAXS data will be the intersection of the spheroid and the plane. Movies illustrating the rotation are provided in the Supporting Information (arg2.avi).

same symmetry would have sharp Bragg spots which lay on these spheres. If, however, one reciprocal space axis was longer than the other two, as in the present case, these spots would lie on concentric shells of prolate spheroids. In scattering techniques, the two-dimensional pattern that is observed is the intersection of the structure factor in reciprocal space with the Ewald sphere. Because we are in the very small angle regime (q_x, q_y < 0.08 Å), the edge of the Ewald sphere is well-approximated by a planar surface. The spheres in reciprocal space would give rise to powder rings that are circular. For the generalization to a reciprocal-space prolate spheroid, the intersection of this spheroid with the Ewald plane must be calculated (Figure 11). As the sample is rotated about an axis, the intersection will trace out ellipses of varying eccentricity (a/b) and orientation (θ_0). (For an illustration, see the movie in the Supporting Information.) Were the spheroid bisected along one of the principal axes, a circle would be formed by the intersection. As the spheroid is rotated, the circle becomes an ellipse with increasing eccentricity; one axis of the ellipse will maintain its original length while the other grows. In the general case where the rotation axis is not along one of the principal axes, ellipses will always be formed. However, these have a similar behavior. When the eccentricity (a/b) is minimal, the ellipse axes coincide with q_x and q_y. Rotating the sample changes the semimajor axis length and, in general, also rotates the ellipse.

Each frame in the rotation series data was least-squares fit with an ellipse that connects the bright ⟨211⟩ peaks. From each ellipse, the length of the semimajor and semiminor axes (a,b) and the offset angle (θ_0) from q_y to the semimajor axis were determined. Qualitatively, several features are immediately apparent. At $\phi = 0°$, a/b is at minimum and $\theta_0 \approx 0°$. Rotating the sample through to $\phi = 90°$, a/b achieves a maximum and the ellipse tilt, θ_0, is also extremal. This follows the stretched q-spheroid model. A more careful test can be performed, and useful information about the strain and sample orientation can be extracted by a quantitative fit. The a/b and θ_0 parameters were independently fitted to the analytic equation for the intersection of an ellipsoid with a plane, as shown in Figure 12. The results are that the major axis of the ellipsoid and

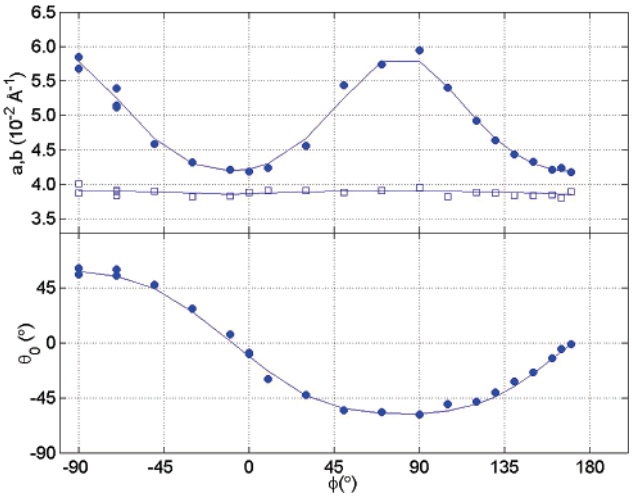

Figure 12. Ellipse parameters dependence on sample rotation ϕ. (a) Lengths of major (●) and minor (□) axes (a,b). (b) Angle (θ_0) between the semimajor ellipse axis and rotation axis q_y. The incident beam direction is along q_z. Points represent results from elliptical fits as illustrated in Figure 9. The continuous curves are the analytic result from the intersection of an ellipsoid and a plane, with parameters determined by least-squares fits to the points.

rotation axis (q_y) are at a relative angle of 60 ± 8° and that the lattice dimensions are approximately 397 ± 8 Å in the plane of the sample face, and 266 ± 4 Å in the surface normal direction. The shrinkage along the film normal amounts to approximately one-third and therefore constitutes a major effect. We have demonstrated the most general case here, where the rotation axis does not coincide with any preferred axis of the ellipsoid. By carefully aligning the sample so that the surface normal coincides with the sample beam direction, no eccentricity is observed. If the sample is then rotated, the eccentricity increases but the ellipses do not rotate ($\theta_0 = \pm 90°$). This special case is consistent with our analysis above. Examples of these rotation series, with smaller angular increments and multiple rotation axes, are available in the Supporting Information. All data are consistent with the interpretation that the samples have shrunk along the sample normal, relative to the two axes parallel to the sample face, for both the as-made and the calcined samples.

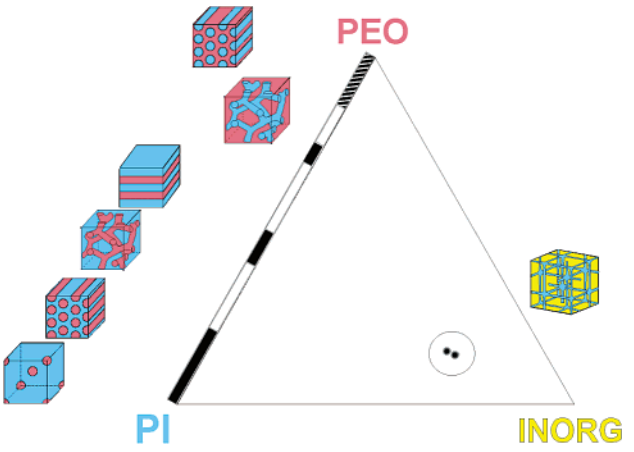

Figure 13. Pseudo-ternary morphology diagram for the present PI-*b*-PEO block copolymer−aluminosilicate nanocomposite materials elucidating the phase space where the two samples with plumber's nightmare morphology were found. Appearance of different phases for the PI-*b*-PEO block copolymer system was taken from Floudas et al.[32] The hatched area corresponds to parts of the PI-*b*-PEO phase diagram that have not yet been experimentally explored.

Pseudo-ternary Morphology Diagram. The pseudo-ternary morphology diagram for the present PI-*b*-PEO block copolymer−aluminosilicate nanocomposites is shown in Figure 13, elucidating the region in phase space where the two samples with plumber's nightmare morphology were found. The appearance of the different phases in the composition space for the pure PI-*b*-PEO block copolymer system in the melt was taken from the phase diagram published by Floudas et al.[32] We refer to the diagram as a pseudo-ternary morphology diagram rather than a ternary phase diagram because the rigid nature of the inorganic network forming upon preparation freezes in a particular morphology and thus prevents transitions between various morphologies observed at different points in phase space. As is evident from Figure 13, between the compositions of the pure block copolymer with double gyroid morphology and PI as the minority and PEO as the majority components and the ternary composition range of the plumber's nightmare with PI as the minority and PEO + inorganic as the majority phase, there is a large area of the phase diagram left open for exploration. Indeed, all morphologies described in previous studies of the present ormocer derived PI-*b*-PEO block copolymer−aluminosilicate nanocomposites [22] were obtained from compositions in the lower, PI-rich part of the ternary morphology diagram in Figure 13.[22,53]

While coexistence regions for double gyroid and plumber's nightmare phases are possible, in principle, analogy to ternary systems amphiphile−water−oil (organic solvent) suggests the potential existence of other bicontinuous structures. As an example, in a study of the system didodecyldimethylammonium bromide−water−styrene, a sequence of five different bicontinuous phases has been reported.[30] The sequence of four of these was proposed to be G ($Ia\bar{3}d$) → D ($Pn\bar{3}m$) → P ($Im\bar{3}m$) → C ($Im\bar{3}m$), the latter phase being based on the Neovius minimal surface (see also Figure 6). It is interesting to note that the analogy with this sequence would suggest the occurrence of a double diamond (D, $Pn\bar{3}m$) structure between the double gyroid (G, $Ia\bar{3}d$) and plumber's nightmare (P, $Im\bar{3}m$) morphologies observed for the pure PI-*b*-PEO and the hybrids discussed in the present paper, respectively. Experiments to elucidate such phase behavior would be extremely valuable. In analogy with the amphiphile−water−oil system, a wide variety of phases can be expected as the stoichiometric ratios of PI, PEO, and inorganic components are varied. In particular, as the ratio of inorganic materials is systematically decreased, transitions into double diamond and then double gyroid phases are anticipated. In this context, it should be noted that a G → D phase transition with the addition of minority component homopolymer into AB diblock copolymer melts and the accumulation of homopolymer at nodes relaxing interfaces to constant mean curvature surfaces favored by the interfacial tension[54] has already been predicted.[46,55] However, models that consider curvature and stretching indicate that the free energy differences between the G, D, and P phases are very slight in many systems.[42,56] Additional considerations may easily alter the hypothesized phase diagrams. This subtlety implies an extreme sensitivity to the details of the interactions and a highly tunable morphology. With the high degree of ordering demonstrated through well-developed X-ray patterns, the present hybrids constitute an ideal model system and thus a unique opportunity to study these fundamental issues in polymer hybrid materials phase science.

Acknowledgment. The financial support of the National Science Foundation (Grant DMR-0072009) and the Department of Energy (DE-FG02-97ER62443) is gratefully acknowledged. The work was further supported by the Cornell Center for Materials Research, a Materials Research Science and Engineering Center of the National Science Foundation (DMR-0079992). The experiments made use of the Cornell High Energy Synchrotron Source (CHESS), which is supported by the NSF and the NIH-National Institute of General Medical Sciences under award DMR-9713424. We thank Jim Hoffman for helpful discussions concerning the construction of the skeletal figures and appropriate level sets that mimic minimal surfaces, Ernie Fontes for experimental assistance at the CHESS D-1 beamline, and Mark Tate for advice and assistance with CCD SAXS detectors.

Supporting Information Available: (1) Rotation-data.mov: This is a sequence of frames corresponding to Figure 9. The sample is rotated about the vertical axis. (2) Ellipse-rotation-.mov: This illustrates the rotation of the ellipsoid of revolution of Figure 11 as it cuts through the Ewald sphere, which is effectively equivalent to a plane of intersection for SAXS being considered. (3) Rotation-calcined.mov: This is a movie of X-ray diffraction of a calcined sample as it is rotated in the X-ray beam. Note the change in the shape of the ellipse as the sample is rotated about the vertical axis. This material is available free of charge via the Internet at http://pubs.acs.org.

JA0355170

(53) Garcia, C. B. W.; Ulrich, R.; Wiesner, U. *Polym. Prepr. (Am. Chem. Soc., Div. Polym. Chem.)* **2002**, *43*, 399; as well as a forthcoming publication by the same authors.

(54) Matsen, M. W. *Phys. Rev. Lett.* **1995**, *74*, 4225−4228.
(55) Matsen, M. W.; Bates, F. S. *Macromolecules* **1996**, *29*, 7641−7644.
(56) Dotera, T. *Phys. Rev. Lett.* **2002**, *89*, art. no.-205502.